



# Effect of Second Phase on the Pitting Corrosion of ZL101A Aluminum Alloy in Thin Electrolyte Layer Environment Containing Cl

Xiaoming Ding<sup>1,2</sup> · Zhen Liu<sup>3</sup> · Qinglin Li<sup>3</sup> · Tianyi Zhang<sup>3</sup> · Chao Liu<sup>3</sup>

Received: 9 September 2021 / Accepted: 26 December 2021 / Published online: 17 January 2022  
© King Fahd University of Petroleum & Minerals 2022

## Abstract

The pitting corrosion of ZL101A aluminum alloy in the thin electrolyte layer containing Cl<sup>-</sup> was studied through the salt spray test. The pitting corrosion behavior was mainly characterized by scanning electron microscopy, electrochemical measurements and in-situ scanning Kelvin probe force microscopy. The results indicated that the second phases in ZL101A aluminum alloy had significant effects on the pitting corrosion behavior. The Al–Si phase acted as an anode phase induced the initiation of corrosion pits, which led to the decrease of polarization resistance (*R*) and the propagation of corrosion pits along the depth direction. Act as cathodic phase, Mg–Si–Fe phase and Si-rich/Al-poor phase have an 800 mV and 660 mV lower Volta potential than the matrix, respectively. The Volta potential difference between Mg–Si–Fe phase and matrix decreased more significantly than that between Si-rich/Al-poor phase and matrix which remained intact with the duration of corrosion. This verified the higher electrochemical stability of Si-rich/Al-poor phase than Mg–Si–Fe phase, which should be related to the presence of Mg and Fe in Mg–Si–Fe phase.

**Keywords** ZL101A aluminum alloy · Pitting corrosion · Second phase · In-situ SKPFM

## 1 Introduction

Aluminum alloys have been widely developed as advanced materials for many fields such as building, electrical, automobile and aircraft manufacturing [1–5]. Moreover, it has been recognized that the properties of aluminum alloy can be improved by adding alloying elements such as Mg, Cu, Zn, Si for further application [1, 4, 6–9]. For example, Al–Si alloys have more excellent casting characteristics, weldability and stamping resistance than pure aluminum due to the presence of Si [1, 10, 11]. However, Al–Si alloys present worse corrosion resistance than pure aluminum, which was

attributed to the enhanced electrochemical inhomogeneity on matrix caused by the composition segregation [8, 9, 11, 12]. Even worse, the degradation of the areas with uneven composition distribution was sensitive to the pitting corrosion, which can lead to unpredictable damages [11–14].

As a typical Al–Si alloy, ZL101A aluminum alloy has been widely reported in many important fields by alloying a small amount of Si and Mg in the cast aluminum to improve the strength, elongation and corrosion resistance [14–16]. However, the intermetallic compounds on ZL101A aluminum alloy generated during manufacturing process can increase the electrochemical heterogeneity, resulting in an increased susceptibility to pitting corrosion [14, 17]. At the same time, it is not clear whether the precipitated phase is used as positive or negative electrode in the corrosion process of ZL101A aluminum alloy [18–21]. For example, Al–Mg–Si precipitated phase was the cathode on AA 6065 aluminum alloy in the initial corrosion process [22]. However, it can be the anode on AA 2024 aluminum alloy during the dissolution process [22]. Eckermann et al. studied the exfoliation-like attack mechanism relationship of Al–Mg–Si alloy and found that the dissolution preferentially occurred in the low-silicon region, confirming the electrochemical difference between the matrix and the heterogeneous phases on aluminum alloy

✉ Tianyi Zhang  
zhangtianyi\_ustb@163.com

✉ Chao Liu  
liuchaoustb@163.com

<sup>1</sup> National Innovation (Qingdao) High Speed Train Material Research Institute Co. LTD., Qingdao 266109, China

<sup>2</sup> School of Materials Science and Engineering, Beihang University, Beijing 100191, China

<sup>3</sup> Corrosion and Protection Center, Institute for Advanced Materials and Technology, University of Science and Technology Beijing, Beijing 100083, China



[23]. Additionally, aluminum alloys were apt to occur pitting corrosion in marine service environment due to the existence of thin electrolyte layer (TEL) containing chloride ions [1, 18–21, 24]. TEL environment with high concentration of  $\text{Cl}^-$  can definitely accelerate the initiation/propagation of corrosion [1, 2, 20, 21, 24, 25]. It has been reported that the initiation of pitting corrosion is related to the localized stress concentration, which is attributed to the different thermal expansion and Young's modulus between the second phases present and the matrix [9, 10, 12]. While, the galvanic corrosion between the second phases and the matrix also deserves to be further revealed. Thus, the investigation on the relationship between the precipitated phases (second phases) and pitting corrosion behavior for ZL101A aluminum alloy should be critical to develop the composition optimization and heat treatment process to meet the material requirements of industrial devices such as pumps and volutes. Electrochemical tests are always considered to estimate the macro electrochemical properties, which is not enough for the observation of local corrosion behavior [20, 24–29]. Thus, the scanning Kelvin probe force microscopy (SKPFM) with a high resolution of about 1 mV in reading the surface potential, associating the classical scanning Kelvin probe method with atomic force microscopy (AFM), can be applied to simultaneously mapping the topography and the Volta potential distribution on conductive materials surfaces in the air to study the in-situ pitting corrosion behavior [20, 26, 27].

Based on the above background, this work focused on the pitting corrosion behavior of ZL101A aluminum alloy in the simulated marine environment (TEL). The corresponding corrosion mechanism was proposed based on the effects of the second phases, which can effectively provide reasonable composition designation for ZL101A aluminum alloy.

## 2 Experimental

### 2.1 Material and Thin Electrolyte Layer Environment

ZL101A aluminum alloy after heat treatment was processed into specimens with the dimension of 10 mm × 10 mm × 4 mm for corrosion test and microstructure observation. The chemical composition (wt.%) determined by adopting chemical analysis is Si 6.69, Mg 0.34, Fe 0.024, Ti 0.12, Sr 0.028, Zn 0.035, Al balance, which can be seen in Table 1. The heat treatment process was carried out in the muffle furnace at  $535 \pm 5$  °C for 12 h, followed by water quenching, placing at room temperature for 8 h and then aging in the muffle furnace at  $155 \pm 5$  °C for 12 h. The surface of ZL101A specimen was ground with SiC paper from 240 to 3000 grades, cleaned in water, degreased with alcohol and acetone, and then dried in cold air [11–15]. The distribution of second phases and the corresponding elemental composition was investigated

**Table 1** EDS results of different positions around the corrosion pit after 5 min corrosion period

Element/Position	Element content (wt.%)			
	1	2	3	4
Al	74.96	55.27	16.61	91.72
Si	18.23	36.96	81.16	4.17
O	6.16	6.67	2.23	4.11
Mg	0.65	1.10	0	0.01

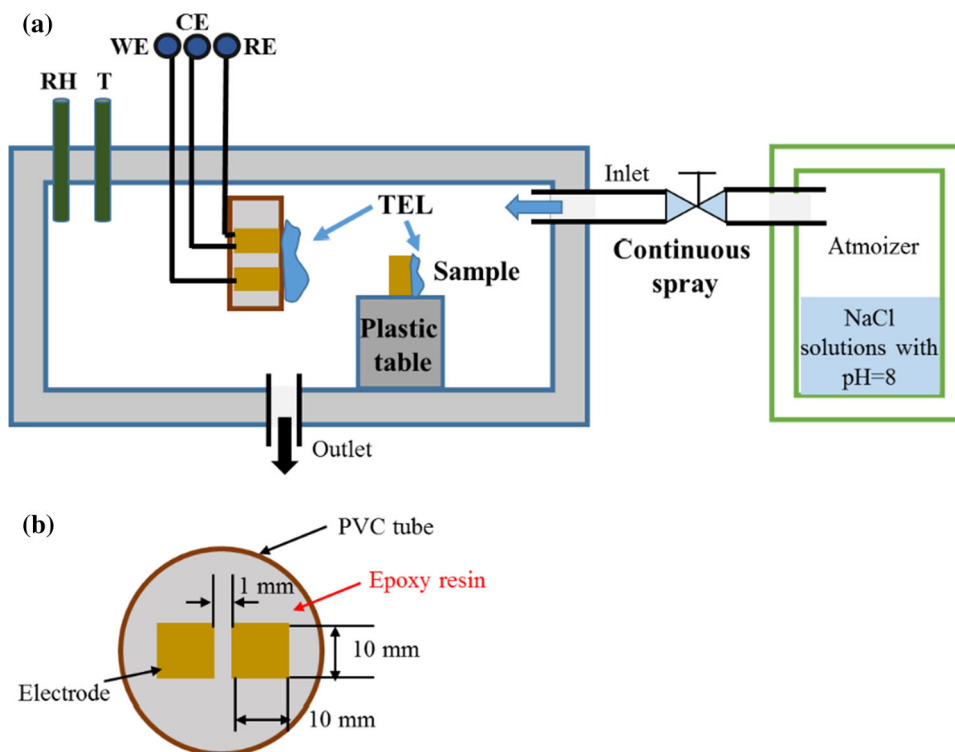
by using a Quanta250 scanning electron microscopy (SEM) equipped with energy dispersive X-ray spectroscopy (EDS). Backscattered electron (BSE) images were obtained with primary electron beam energy of 20 keV to give brightness contrast between different microstructures.

Based on the GBT2423.17-93 and the related researches [1–4], a near neutral 3.5 wt.% NaCl solution (pH = 8) was selected for the salt spray test to make the thin electrolyte layer (TEL) environment. The schematic diagram of the device can be seen in Fig. 1. The test spray was injected into the device for 5 min in advance to produce a stable TEL environment. The ambient temperature and the relative humidity (RH) were set as the indoor temperature ( $24 \pm 2$  °C) and 100%, respectively. The corrosion periods were made up of 5 min, 30 min, 12 h and 72 h. The morphology of corrosion pit and the composition of corrosion products were detected by using SEM and EDS after each corrosion period. Corroded samples were ultrasonically cleaned in concentrated nitric acid for 5 min, then cleaned with water and alcohol and dried in air [11–15]. After that, a confocal laser scanning microscopy (CLSM, KEYENCE VK-X250) was applied for the observation and the statistics of corrosion pits on the sample surface.

### 2.2 Electrochemical Measurement and SKPFM Test

The sample with the dimension of 10 mm × 10 mm × 4 mm was coated with epoxy, leaving an exposure area of 1 cm<sup>2</sup> for electrochemical measurements. It should be mentioned that the double electrode system was used for potentiodynamic polarization test and electrochemical impedance spectroscopy (EIS) test in this work, as shown in Fig. 1b. The double electrode system includes two identical specimens, one of which is the working electrode (WE), and the other is designated as the reference electrode (RE) and counter electrode (CE) simultaneously. According to the previous study [1], the distance of the parallelly arranged electrodes was set as 1 mm. The potentiodynamic polarization curve was measured by using a Gamry Interface 1010E workstation, and the polarization curves was

**Fig. 1 a** The schematic diagram of the designed device for corrosion test and electrochemical measurement and **b** the structure of double electrode system



scanned from  $-1.0$  to  $1.0$   $V_{SCE}$  with the scanning rate of  $0.167$  mV/s. EIS tests were carried out at open circuit potential (OCP) over the frequency range from  $100$  kHz to  $10$  MHz, with imposing a sinusoidal perturbation of  $20$  mV. The obtained data were fitted by using the ZSimpWin software.

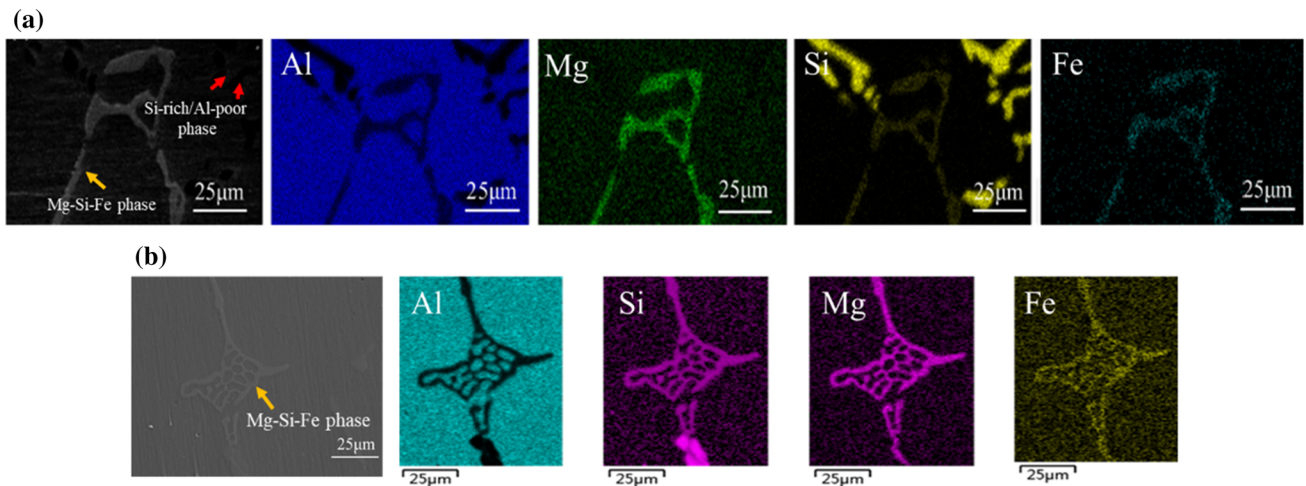
For in-situ observing the local Volta potential differences between the second phase and ZL101A matrix, scanning Kelvin probe force microscopy (SKPFM) tests were conducted on samples after the salt spray test with different corrosion periods, which were finished by using an atomic force microscopy (AFM, Bruker Multimode). Before the in-situ test, samples were polished by the  $0.2\text{-}\mu\text{m}$ -diamond paste and ultrasonically cleaned in the isopropanol for  $5$  min, aiming at reducing the adverse impact of scratches on the local Volta potential distribution. For the convenience of observing, the in-situ observation area was marked by three hardness indentations around the second phases. The surface Volta potential distribution maps were obtained in the air condition ( $25\text{--}30\%$  RH) under the employing the dual-scan mode, including the first pass for obtaining the topography data and the second pass for obtaining the Volta potential data. As for the second scanning pass, the cantilever of the tip was lifted up  $50$  nm to decrease the influence of topographic features on the potential mapping [9, 27–30].

## 3 Results and Discussion

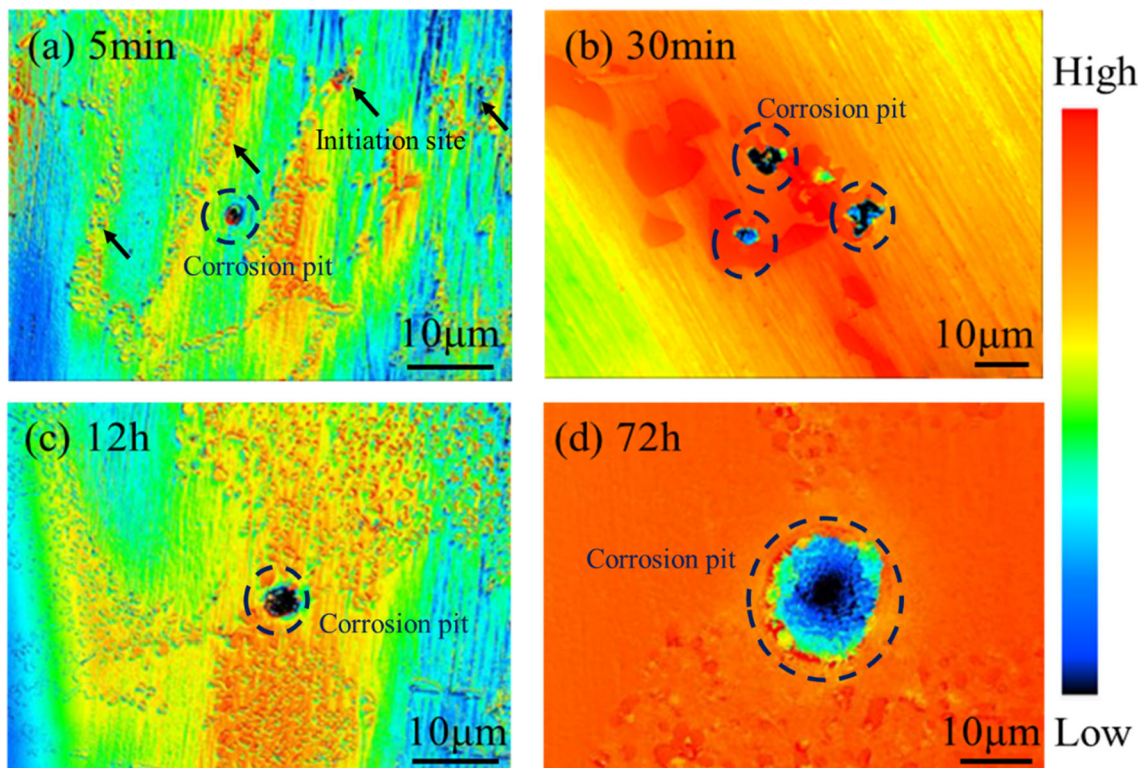
### 3.1 In-Situ Observation of Pitting Corrosion Process in TEL

Figure 2 shows the SEM morphologies and element distributions of the second phases in ZL101A aluminum alloy. It can be found that the second phases are mainly consisted of Mg–Si–Fe phase and Si-rich/Al-poor phase, which present different shapes and size. The two second phases can be distinguished by the existence of Mg and Fe or not in EDS results. Although Fe and Mg are low in content, both elements are involved in the precipitation of the Mg–Si–Fe phase, suggesting the high activity of Fe and Mg in ZL101A aluminum alloy. Both the Si-rich/Al-poor phases and the Mg–Si–Fe phases present block structure. Mg–Si–Fe phases are more continuous than Si-rich/Al-poor phase, suggesting a greater adverse influence of Mg–Si–Fe phases on the uneven elements distribution on ZL101A aluminum alloy, which may lead to different corrosion features.

Figure 3 presents the 3D profiles of the ZL101A aluminum alloy with different corrosion periods after removing corrosion products. As shown in the color scale bar, red represents the high horizontal position, and blue represents the low horizontal position, respectively. For  $5$  min in TEL environment, some distinguishable corrosion initiation sites and generated corrosion pits can be found in Fig. 3a [31–34]. Those initiation sites are mostly distributed around the high horizontal



**Fig. 2** SEM images and EDS mapping results of **a** Si-rich/Al-poor phase and **b** Mg-Si-Fe phase and in ZL101A aluminum alloy



**Fig. 3** Surface topography of ZL101A after corrosion tests with different periods: **a** 5 min **b** 30 min **c** 12 h **d** 72 h

positions, which should be related to the second phases [1, 26, 33–35]. The corrosion pits surrounded by the red areas gradually propagate along the radial direction after 30 min corrosion period. Combined with the microstructures shown in Fig. 2, the red areas can be determined as the second phases, which present a better corrosion resistance compared with the matrix. After 12 h corrosion period, both the number of corrosion initiation sites and the size of corrosion pits increase, indicating the occurrence of localized corrosion

with time in TEL. The consistent result is also found after 72 h corrosion period, as shown in Fig. 3d, indicating the required discussion about the specific influence of the second phases on the pitting corrosion of ZL101A aluminum alloy.

For further analyzing the growth mechanism of corrosion pits, the ratio of the pit depth to the pit diameter recorded as the depth width ratio ( $k$ ) was calculated. There is a linear

relationship between the  $k$  and the pit volume ( $V$ ), which can be expressed as follows [1, 2, 19]:

$$k = tV + b \quad (1)$$

where  $t$  and  $b$  are constants. The fitted results present low error values ( $r^2 < 0.2$ ). When the slope is negative, i.e.,  $t < 0$ ,  $k$  decreases with the increase of  $V$ , representing that the corrosion pits propagate along the depth direction. When the slope is positive, that is,  $t > 0$ ,  $k$  increases with the increase of  $V$ , representing that the corrosion pits propagate along the radial direction (parallel to the sample surface). Figure 4 displays the  $k$ -value diagrams of ZL101A aluminum alloy after different corrosion periods in TEL environment. It can be found that the slope values of curves are negative and increase with time, which indicates that the corrosion pits grow along the depth direction at a high rate during the initial corrosion process, and then at a slower rate during the stable corrosion process.

Figure 5 shows the corrosion morphologies of ZL101A aluminum alloy in TEL environment with different corrosion periods. It can be seen that the corrosion pits are mainly distributed around the second phases, which is consistent with previous studies [20, 21, 24–26, 31–33, 35]. As shown in Fig. 5a and b, corrosion pits expand radially from 5 to 30 min, leaving some second phases around the pits, which should be related to the galvanic corrosion there [23, 25, 33, 34]. The corrosion pits are mainly on the phase with light color instead of the surrounding phase with deep color, which can be interpreted that the corrosion occurred primarily at the area with lower potential. With the increase of corrosion period, the second phases are finally detached from the matrix, as shown in Fig. 5c and d, which is related to the preferential corrosion at the edges between the second phases and the matrix. The above results confirm that the second phases can be divided into the cathode intermetallic (deep color phase) and the anode intermetallic (light color phase) compared to the ZL101A matrix, resulting in different forms of corrosion pits, which needs further explanation.

Figure 6 shows the in-situ SEM morphology of corrosion pits and the EDS point scanning results at different positions of ZL101A aluminum alloy after 5 min corrosion period. The element contents of different positions are listed in Table 1. It can be seen that the corrosion pit is preferentially formed at position 1, which is surrounded by the light color phase. The EDS result of position 2 shows that the light color phase contains 55.27 wt.% Al and 36.96 wt.% Si, which is corresponded to the Al–Si phase. Because of the certain amount of Si in Al–Si phase, this phase may be considered as the Si-rich/Al-poor phase in the microstructure, which causes the unapparent observation of Al–Si phase in Fig. 2. It should be pointed out that the Al–Si phase contains some O and Mg, which are considered as the impurity elements for the

**Table 2** EDS results of different positions around the corrosion pit after 30 min corrosion period

Element/Position	Element content (wt.%)			
	1	2	3	4
Al	66.94	62.48	14.29	92.70
Si	28.07	32.25	84.37	1.85
O	4.16	4.58	1.33	5.37
Mg	0.83	0.69	0	0.09

ZL101A aluminum alloy. The EDS result of position 3 shows that the dark color second phase is the Si-rich/Al-poor phase, containing 16.16 wt.% Al and 81.16 wt.% Si, which surrounds around the Al–Si phase. For comparison, position 4 represents the EDS results of the ZL101A matrix, whose content is basically the same with the actual chemical composition. It can be concluded from the above result that the corrosion pits initiated on the light color Al–Si phase, which is surrounded by the dark color Si-rich/Al-poor phase. There is no corrosion occurred on the Si-rich/Al-poor phase after 5 min corrosion period in TEL environment, suggesting that the Si-rich/Al-poor phase presents better corrosion resistance than the Al–Si phase.

Figure 7 shows the SEM morphology and EDS results of ZL101A aluminum alloy after 30 min corrosion period. Table 2 lists the EDS statistical results at different positions around the corrosion pits. It can be seen from that the number of corrosion pits increases with time in the same magnification field of view, and the corrosion pits tend to merge together to form larger ones (area near the point 1), which should be related to the connection between the Al–Si phase and the corrosion pits. As shown in Table 2, Mg contents are almost zero in the Si-rich/Al-poor phase (point 3) and the matrix (point 4), while the Al–Si phase (point 2) presents 0.69 wt.% Mg, which further proves the existence of Al–Si phase combined with Fig. 6. Thus, it can be detected that the self-dissolution occurred preferentially on Al–Si phase during the corrosion test in TEL environment; confirming the lower stability of Al–Si phase than the Si-rich/Al-poor phase and the matrix. In the center of corrosion pit (point 1), Mg content presents a relatively high content, which should be related to the dissolution of Al–Si phase, and the accumulation of corrosion products containing Mg. Therefore, it can be speculated that the higher dissolution activity of Al–Si phase is closely related to the existence of Mg, which is consistent with the results shown in Fig. 6 and Table 1.

Figure 8 is the SEM morphology and EDS point scanning results of the corrosion pit on ZL101A aluminum alloy after 12 h corrosion period in TEL environment. Table 3 lists the EDS statistical results at different positions around the corrosion pits. It can be seen that the bottom of corrosion

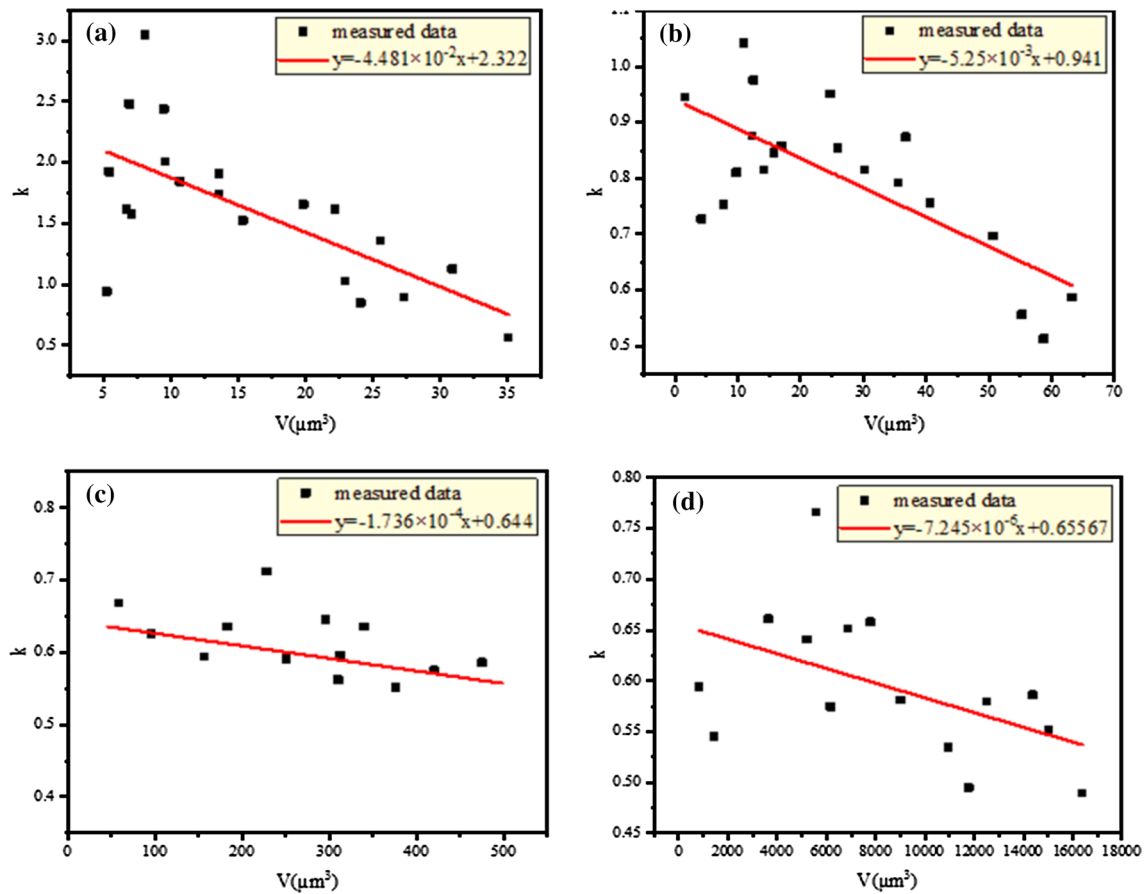


**Fig. 4** The  $k$ -value diagrams of ZL101A aluminum alloy after corrosion tests with different periods in TEL environment: **a** 5 min **b** 30 min **c** 12 h **d** 72 h

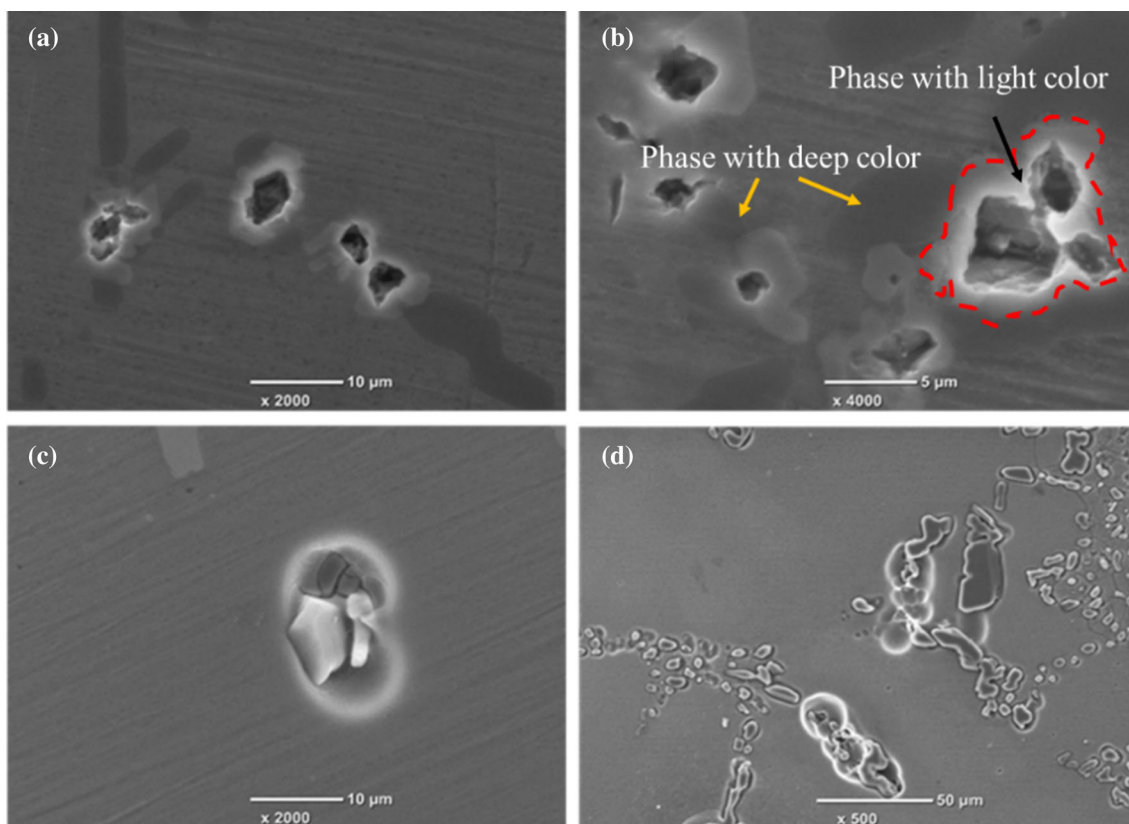
pit presents some cracks. Some undissolved second phases are found in the center of the corrosion pit (point 1), which are detected as the Si-rich/Al-poor phase by EDS results, containing 7.9 wt.% Al and 87.74 wt.% Si. The corrosion pits gradually grow together with the dissolution of Al–Si phase, leaving the Si-rich/Al-poor phase in the center of the corrosion pit, which confirms that the Si-rich/Al-poor phase and the Al–Si phase are close and interdependent. It should be noted that two Si-rich/Al-poor phases are separated by a gully, which should be filled with the Al–Si phase before the corrosion based on the former results, suggesting the anode role of Al–Si phase during corrosion test. The Si-rich/Al-poor phase presents a lighter color after 12 h than 5 min and 30 min, which may be related to the gradually increased activity of the Si-rich/Al-poor phase during corrosion process.

Figure 9 shows the SEM image and EDS point scanning results of the corrosion pit on ZL101A aluminum alloy after 72 h corrosion period in TEL environment. Table 4 lists the EDS statistical results at different positions around the corrosion pits. It can be seen that the corrosion pit after 72 h presents the similar morphology with the 12 h corrosion period. The remained Al–Si phase at the edge of corrosion

**Table 3** EDS results of different positions around the corrosion pit after 12 h corrosion period

Element/Position	Element content (wt.%)		
	1	2	3
Al	7.90	77.15	90.43
Si	87.74	4.40	0.71
O	4.31	18.14	8.55
Mg	0.05	0.30	0.31

pit gradually decreases with time, which confirms the higher dissolution activity of Al–Si phase than the Si-rich/Al-poor phase. The Mg content of matrix gradually increases with time from 12 to 72 h, as listed in Tables 3 and 4, which should be related to the dissolution of matrix and the accumulation of Mg element. Thus, the adverse effect of Mg on the stability of ZL101A aluminum alloy is confirmed. Meanwhile, the pitting corrosion behavior of ZL101A aluminum alloy is determined by different second phases. Al–Si phase can dissolve to accelerate the formation of initiation sites for corrosion pits during corrosion process. While, the effects of the



**Fig. 5** Corrosion morphology (SEM: backscattered electron pattern) of ZL101A aluminum alloy after different corrosion periods: **a** 5 min, **b** 30 min, **c** 12 h, **d** 72 h

**Table 4** EDS results of different positions around the corrosion pit after 72 h corrosion period

Element/Position	Element content (wt.%)		
	1	2	3
Position			
Al	3.48	82.79	92.51
Si	94.12	14.55	0.82
O	2.35	2.66	6.10
Mg	0.05	0	0.58

Si-rich/Al-poor phase and Mg–Si–Fe phase on the corrosion behavior deserve further discussion.

### 3.2 Electrochemical Tests and Analyses

For further characterizing the long-term corrosion behavior of ZL101A in TEL environment, Fig. 10 displays the potentiodynamic polarization curves with different corrosion periods. Pitting corrosion potential ( $E_{pit}$ ), corrosion potential ( $E_{corr}$ ) and corrosion current density ( $I_{corr}$ ) obtained by the fitted of potentiodynamic polarization curves are listed in Table 5. It can be found that three curves present similar shape, suggesting a basically same electrochemical mech-

**Table 5** Fitted data of the potentiodynamic polarization curves after different corrosion periods

Corrosion period	12 h	72 h	120 h
$E_{corr}$ (V <sub>SCE</sub> )	0.089	0.112	− 0.185
$I_{corr}$ (mA/cm <sup>2</sup> )	2.025E+4	1.611E+4	1.049E+4
$E_{pit}$ (V <sub>SCE</sub> )	0.752	0.754	0.751

anism [25]. The cathode region is controlled by oxygen diffusion process, and the anode region is controlled by the active dissolution process. The anode branches are in an active dissolution state in TEL environment for all periods, leading to an inconspicuous passivation range [23, 25–34]. With the extension of corrosion time,  $E_{corr}$  decrease from 12 to 120 h, which indicates the accumulation of active substances on sample surface [25–29]. Combined with the in-situ EDS results, the active substances should be the corrosion products containing Mg and Al. The similar evolutions of  $I_{corr}$  and  $E_{pit}$  confirm the severe corrosion condition of the TEL environment, which causes the hard distinguish of the corrosion resistance after different corrosion periods.

For characterizing the evolution of corrosion resistance, Fig. 11 illustrates the EIS results of ZL101A aluminum alloy

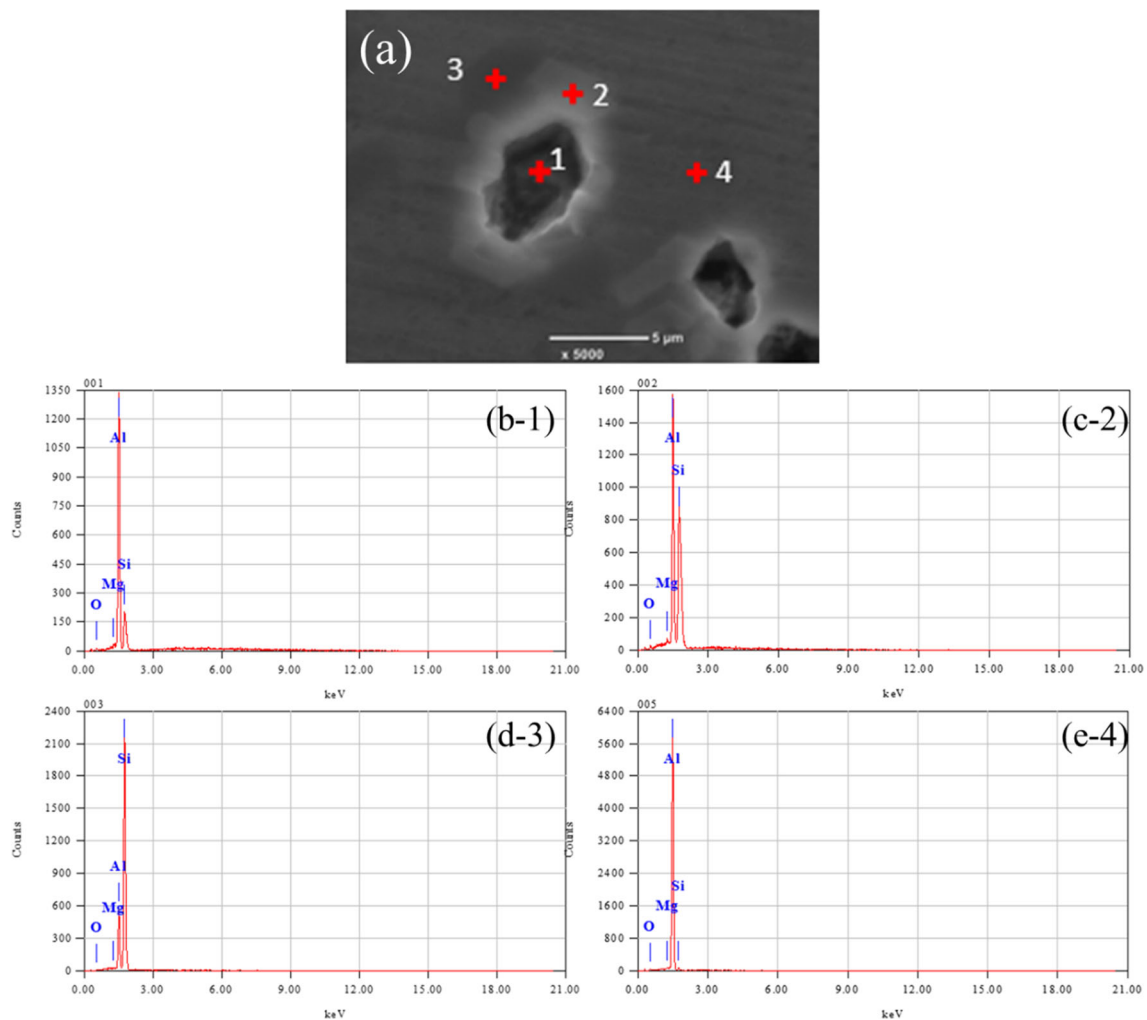


**Fig. 6** SEM image of corrosion pits and EDS results at different positions after 5 min corrosion period: **a** SEM image, **b** position 1, **c** position 2, **d** position 3, **e** position 4

after 12 h, 72 h and 120 h in TEL environment. It can be seen from the Nyquist plots that the impedance spectrum are basically the same in three periods, including a large capacitive reactance arc in the high frequency region representing the charge transfer process and a small capacitive reactance arc in the medium- and low-frequency region representing the protectiveness of the corrosion product film, respectively [1, 11, 14]. The capacitance arc radius of film is smaller than that of the double layer capacitance, which indicates that the double layer plays a leading role during the corrosion process in TEL environment. The decrease of the capacitance arc radius indicates the degradation of ZL101A aluminum alloy with time in TEL environment, which can intensify the pitting corrosion, as shown in Fig. 3. As shown in the EIS Bode diagram in Fig. 11b, the phase angle curves present a wide peak in the intermediate frequency region (10–1000 Hz), which is consistent with the two time constants, corresponding to the two capacitance arcs in Nyquist plots [12–14].  $|Z|_{0.01}$  as a

quantitative index for evaluating the protectiveness of the film [25] gradually decreases with corrosion time, which shows the same evolution with  $k$ -value, as shown in Fig. 4.

Further, the EIS fitted parameters are finished by using the R(Q(R(QR))) equivalent circuit (Fig. 11c) and listed in Table 6. Specifically,  $R_f$  and  $Q_f$  represent the resistance and capacitance of the corrosion product film, respectively.  $R_{ct}$  and  $Q_{ct}$  represent the resistance and capacitance of the electric double layer, respectively.  $R_s$  is the solution resistance. Due to the dispersion effect caused by the accumulation of corrosion products on the sample surface, the constant phase angle element (CPE) of impedance can be calculated by the following formula [14, 35–40]:

$$Z_{CPE} = [Q(jw)^n]^{-1} \quad (2)$$

where  $Q$  is the capacitance of CPE,  $n$  is the CPE index and represents the degree of dispersion effect, correspond-



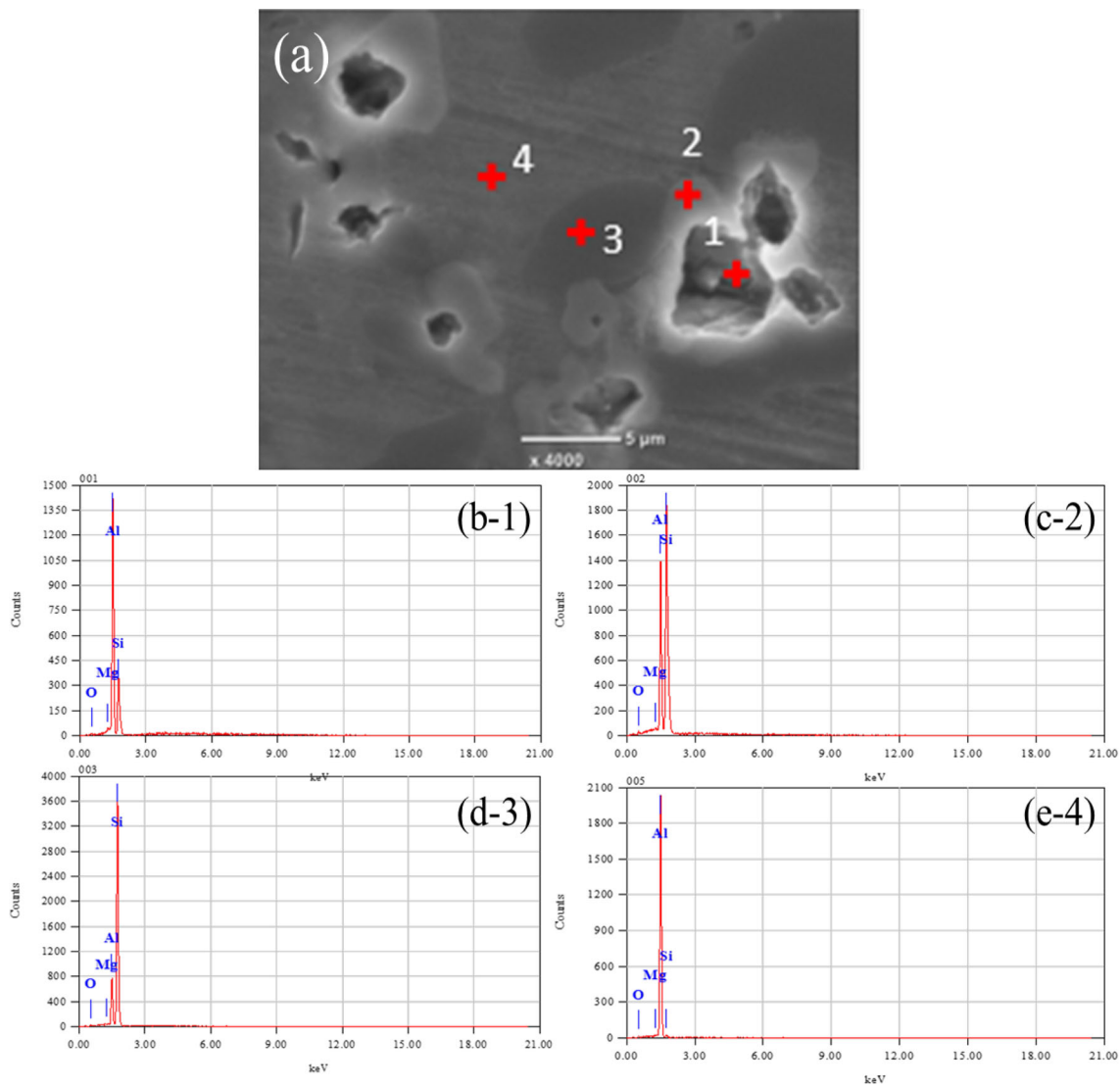


**Fig. 7** SEM image of corrosion pits and EDS results at different positions after 30 min corrosion period: **a** SEM image, **b** position 1, **c** position 2, **d** position 3, **e** position 4

**Table 6** Fitted parameters of the EIS results after corrosion tests with different periods

	12 h	72 h	120 h
$R_s/\Omega\cdot\text{cm}^{-2}$	16.20	13.45	12.95
$R_{ct}/\Omega\cdot\text{cm}^2$	$2.025\text{E} + 4$	$1.611\text{E} + 4$	$1.049\text{E} + 4$
$Q_{dl}/\mu\text{F}\cdot\text{cm}^{-2}$	$6.149\text{E}-4$	$1.457\text{E}-3$	$6.523\text{E}-4$
$n_{ct}$	0.85	0.82	0.81
$R_f/\Omega\cdot\text{cm}^{-2}$	$5.499\text{E} + 3$	$3.331\text{E} + 3$	$4.937\text{E} + 3$
$Q_f/\mu\text{F}\cdot\text{cm}^{-2}$	$7.222\text{E}-6$	$1.211\text{E}-5$	$2.185\text{E}-5$
$n_f$	0.90	0.78	0.75

ing to  $n_f$  and  $n_{ct}$ ,  $w$  is the angular frequency,  $j^2 = -1$ . It can be found that the polarization resistance  $R$  ( $R_f + R_{ct}$ ) decreases gradually with time, corresponding to the evolu-

tion of  $|Z|_{0,01}$ , which confirms that the corrosion resistance of ZL101A aluminum alloy decreases gradually with time in the TEL environment. Comprehensively, the dissolution of matrix and second phases should be the direct inducement for the degeneration of ZL101A aluminum alloy in TEL, which deserves detailed discussion in the following part.

### 3.3 In-Situ SKPFM Observation and Analyses

In order to in-situ explore the influence of the second phase on the pitting corrosion behavior of ZL101A aluminum alloy in TEL environment, SKPFM tests were carried out on the samples after 5 min, 30 min, 3.5 h corrosion periods. The sur-

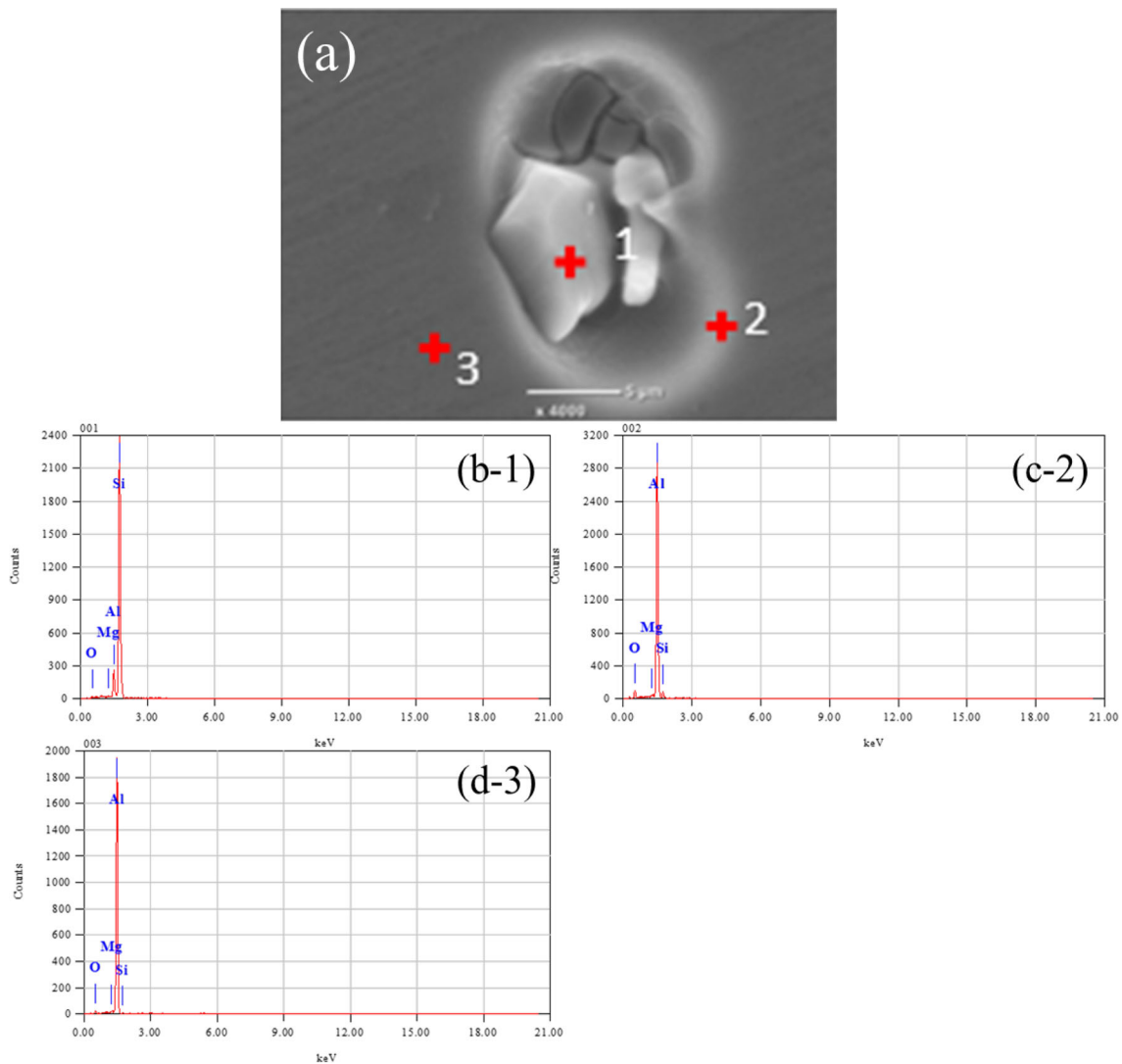


**Fig. 8** SEM image of corrosion pits and EDS results at different positions after 12 h corrosion period: **a** SEM image, **b** position 1, **c** position 2, **d** position 3

face potential difference between the tip and sample surface is defined as follows [3, 20, 28–30, 32]:

$$V_{\text{volta}} = \frac{\phi_{\text{tip}} - \phi_{\text{sample}}}{e} \quad (3)$$

where  $\phi_{\text{tip}}$  and  $\phi_{\text{sample}}$  are the work functions of the tip and the sample, respectively,  $e$  is the electron charge, and then  $V_{\text{volta}}$  is the surface potential difference [3, 12, 20, 21, 28–30, 32]. Higher  $V_{\text{volta}}$  represents higher absolute potential for the substance. It can be summarized from the 3.2 part that the Al–Si phase acted as an anode can provide a driving force for the local galvanic corrosion [1, 2, 11] and promote the initiation of corrosion pit on itself. While, the effects of Mg–Si–Fe phase and Si-rich/Al-poor phase on corrosion have not been clarified. Therefore, the obtained Volta potential distribution maps and the corresponding line profiles of Mg–Si–Fe phase

are presented in Fig. 12. It can be found that the Mg–Si–Fe phase is significantly brighter than the matrix in Fig. 12a, which indicates the higher Volta potential of Mg–Si–Fe phase than matrix initially. The differences between the potential of Mg–Si–Fe phase and the average potential of matrix are about 700 mV, as shown in Fig. 12e, suggesting the enough energy for the initial local galvanic corrosion [20, 21]. Therefore, Mg–Si–Fe phase acted as a cathode phase can promote the preferential dissolution of the surrounding area of Mg–Si–Fe phase at the initial corrosion stage. With the extension of time, the Volta potential difference between the Mg–Si–Fe phase and the matrix gradually decreases from 5 min to 3.5 h, which are 470 mV in Fig. 12f, 260 mV in Fig. 12g and 290 mV in Fig. 12h. It should be noticed that the Volta potential of the Mg–Si–Fe phase presents an unstable line profiles, corresponding to the gradually blurred Volta poten-

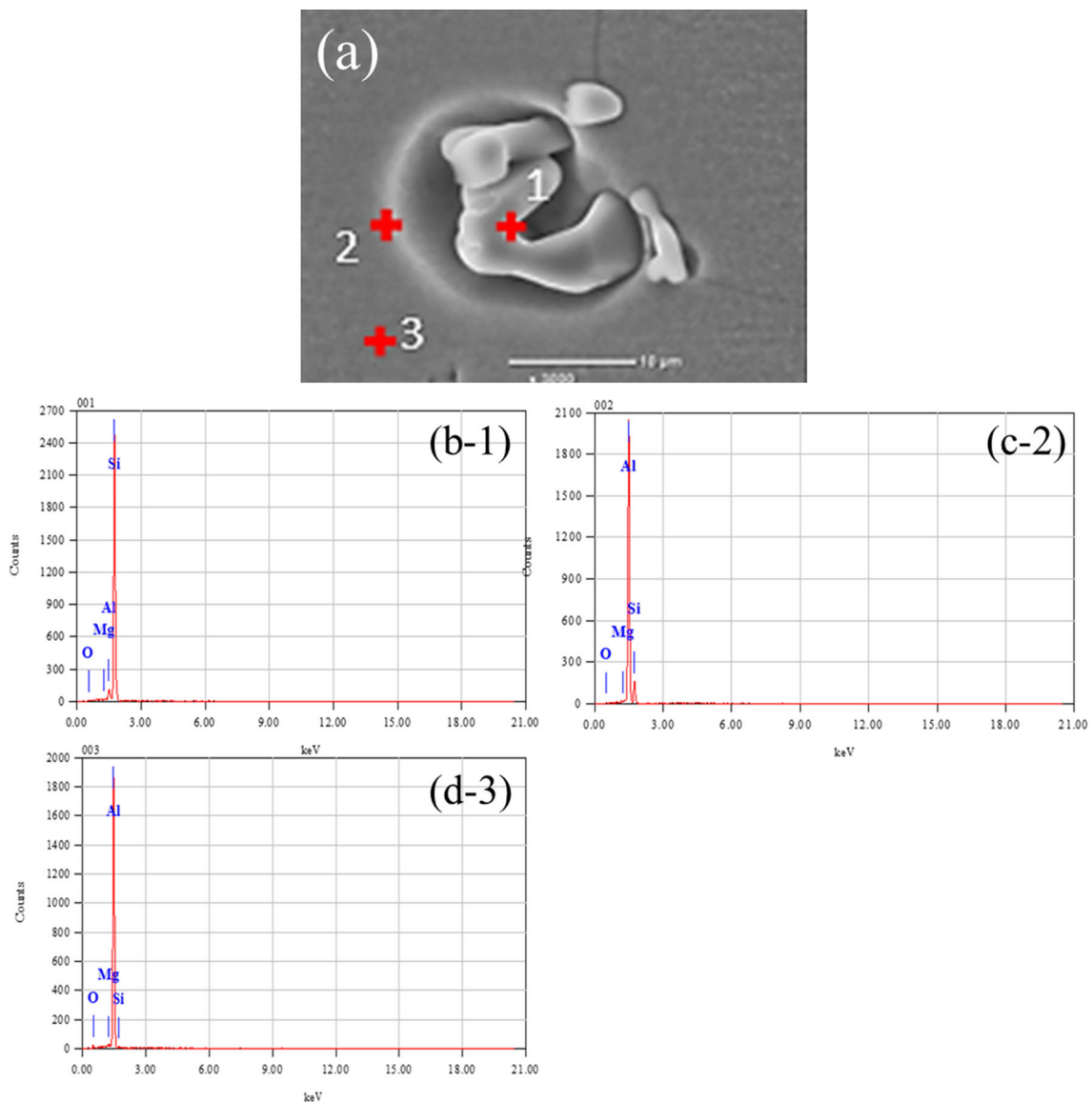


**Fig. 9** SEM image of corrosion pits and EDS results at different positions after 72 h corrosion period: **a** SEM image, **b** position 1, **c** position 2, **d** position 3

tial distribution Maps. The decrease of the Volta potential difference between the Mg–Si–Fe phase and the matrix gradually indicates the weakened galvanic corrosion effect there. The decreased Volta potential stability of Mg–Si–Fe phase suggests the dissolution of Mg–Si–Fe phase in TEL environment. Combined with the EDS results, the dissolution should be related to existence of Mg and Fe elements in the phase, which confirms that both Mg and Fe are not conducive to the stability of the second phases in ZL101A aluminum alloy. It can be further inferred that the dissolution of Mg–Si–Fe phase can cause the enhanced local corrosion, leading to the formation of corrosion pits, as shown in Fig. 5.

Figure 13 shows the SKPFM results of the Si-rich/Al-poor phase after different corrosion periods in TEL environment.

The results show that the Volta potential of Si-rich/Al-poor phase is about 625 mV higher than that of matrix, which confirms the cathode role of the Si-rich/Al-poor phase during corrosion [27, 28, 32, 34]. The variation of the Volta potential difference between the Si-rich/Al-poor phase and the matrix changes slightly with time, which are about 500 mV in Fig. 13f, about 500 mV in Fig. 13g and about 350 mV in Fig. 13h. The Si-rich/Al-poor phase presents gradually unstable potential maps with the increases of time, which indicates that a certain degree of dissolution occurred in TEL environment. While, the Volta potential difference between the Si-rich/Al-poor phase and the matrix remains obvious during four corrosion periods compared with the Mg–Si–Fe phase, which also verifies the adverse effects of Mg and Fe

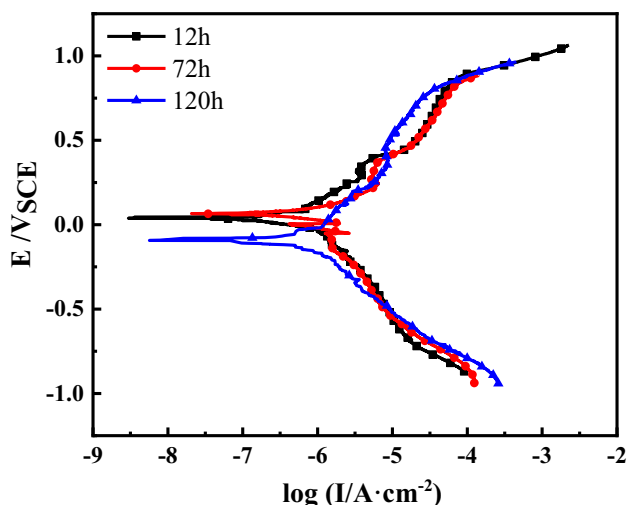


**Fig. 10** Potentiodynamic polarization curves of the ZL101A in TEL environment with different periods

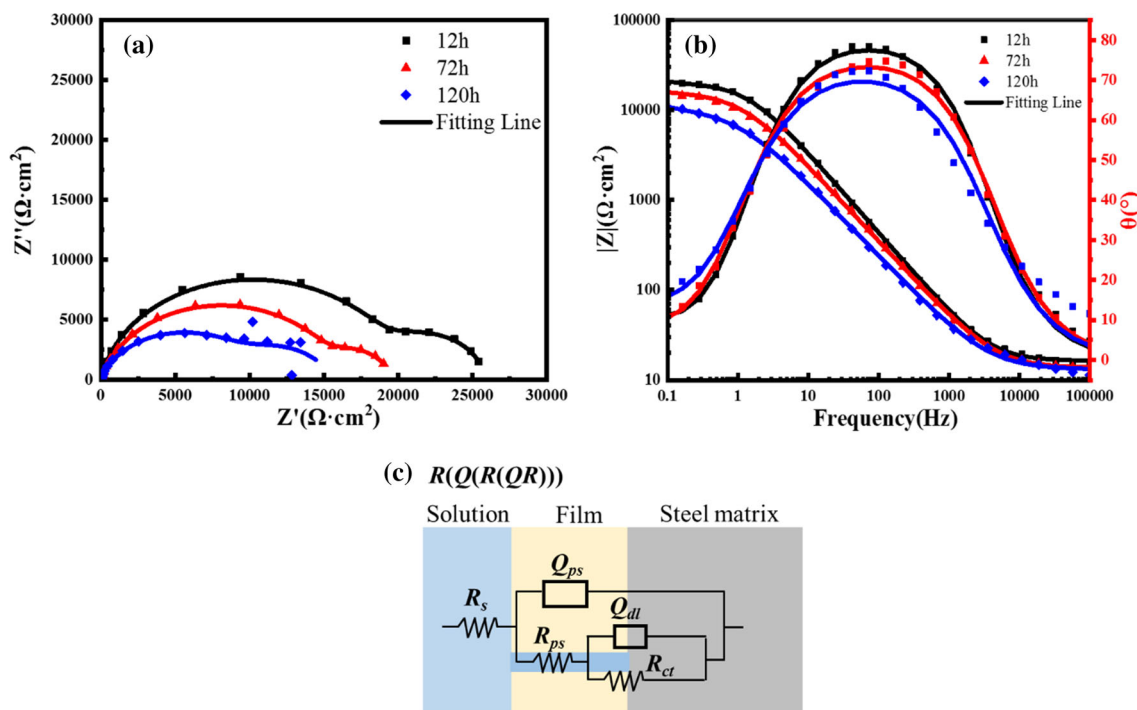
on the stability of second phase. This led to the preferential dissolution of the area surrounding the Si-rich/Al-poor phase and the corrosion gully, corresponding to the results shown in Figs. 8 and 9. The local galvanic corrosion caused by the Si-rich/Al-poor phase belongs to the type of small cathode and large anode [32, 34], which is contributed to the inconspicuous uniform corrosion instead of the pitting corrosion, contrasting to the type of large anode and small cathode

caused by the Al–Si phase. Thus, both the proportion of Al and Si and the existence of Mg and Fe had effects on the corrosion resistance of the second phase.

Based on the analyses above, the schematic diagram illustrated in Fig. 14 describes the mechanism of the pitting corrosion process of the ZL101A aluminum alloys in TEL environment. Firstly, the Al–Si phase with higher proportion of Al was more prone to corrosion than the Si-rich/Al-poor phase, contributing to the high activity of Al than Si. The dissolution of the Al–Si phase was the main reason for the formation of corrosion pits. Secondly, the sites containing Mg can be divided into two categories, including the active areas containing Mg on matrix and second phase and the corrosion products containing Mg. With the progress of corrosion, those active sites were evolved into corrosion initiation sites through the dissolution of itself in TEL environment, which results in the uniform corrosion on sample surface.

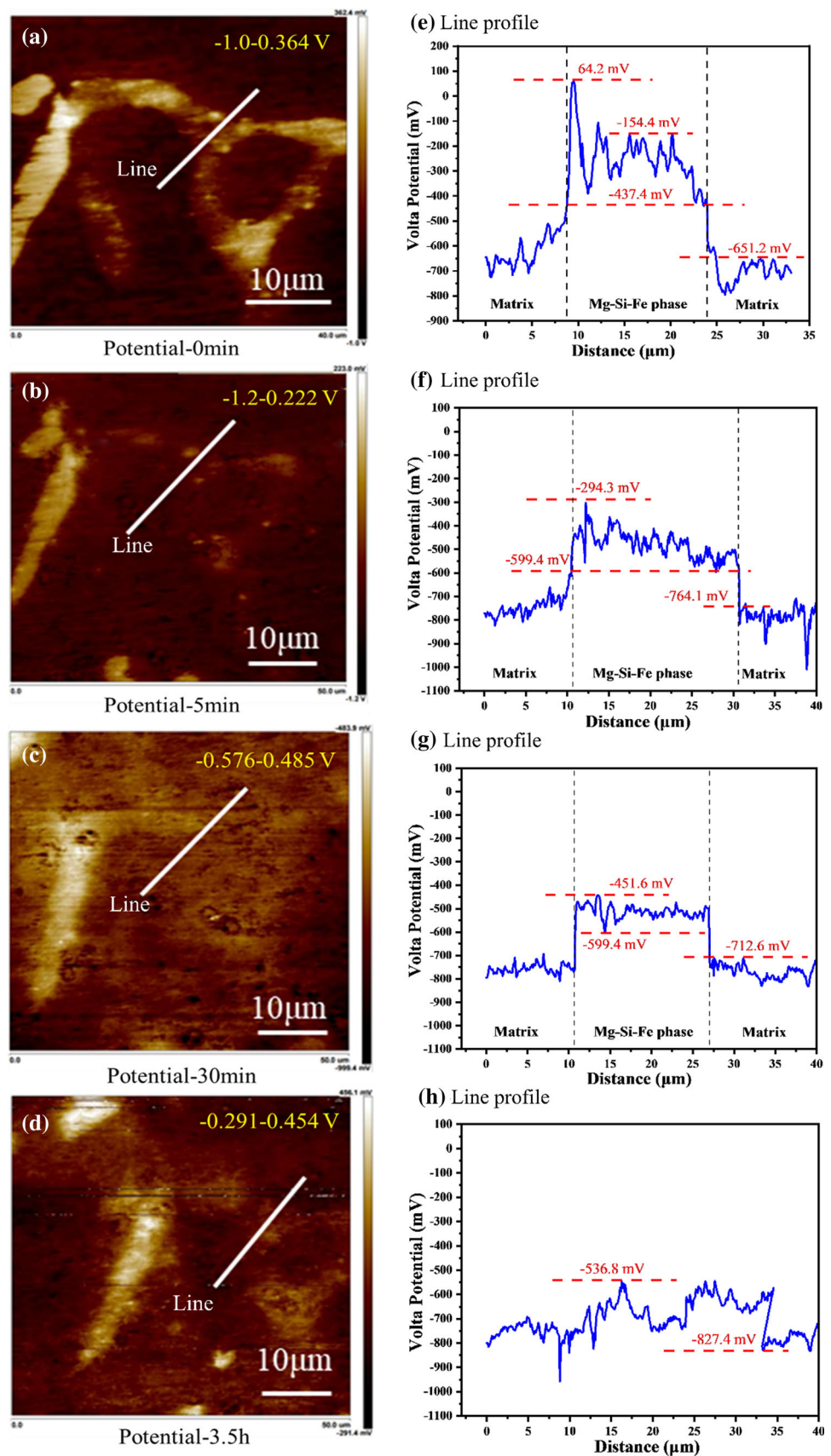
## 4 Conclusion

Three kinds of second phases including Al–Si phase, Si-rich/Al-poor phase and Mg–Si–Fe phase were found in the ZL101A aluminum alloy, which were dispersed on the matrix in forms of blocks and strips. Al–Si phase served as the anode and was contributed to the initiation and development of corrosion pits during the corrosion process, which should be

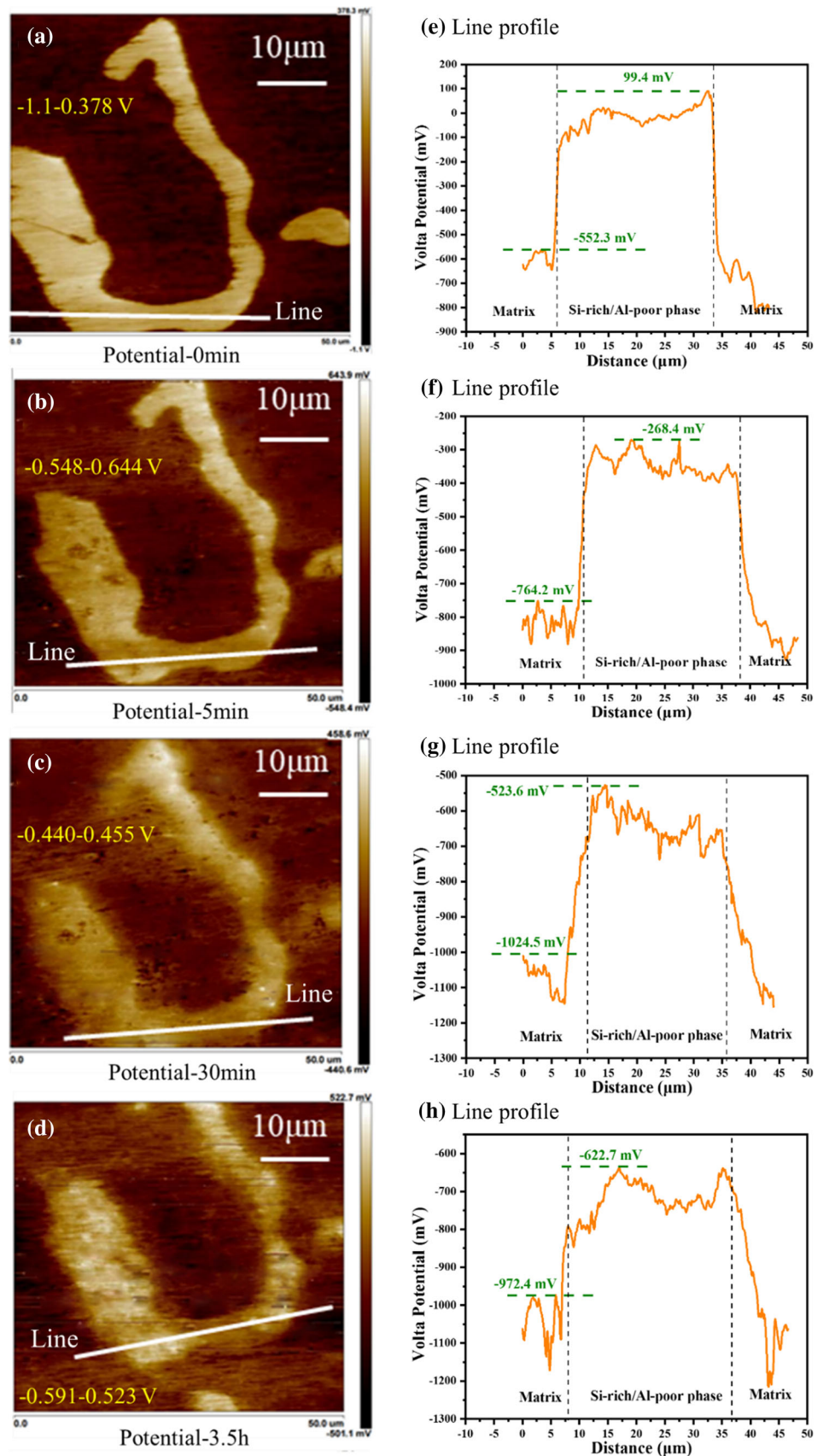


**Fig. 11** Electrochemical impedance results of the ZL101A during the corrosion test in TEL environment with different periods: **a** Nyquist plots, **b** Bode diagrams, **c** equivalent circuit

**Fig. 12** SKPFM results of the Mg-Si-Fe phase after corrosion test with different periods. Volta potential distribution maps: **a** 0 min, **b** 5 min, **c** 30 min, **d** 3.5 h, Volta potential linear profiles of Mg-Si-Fe phase: **e** 0 min, **f** 5 min, **g** 30 min, **h** 3.5 h



**Fig. 13** SKPFM results of the Si-rich/Al-poor phase after corrosion test with different periods. Volta potential distribution maps: **a** 0 min, **b** 5 min, **c** 30 min, **d** 3.5 h, Volta potential linear profiles of Si-rich/Al-poor phase: **e** 0 min, **f** 5 min, **g** 30 min, **h** 3.5 h



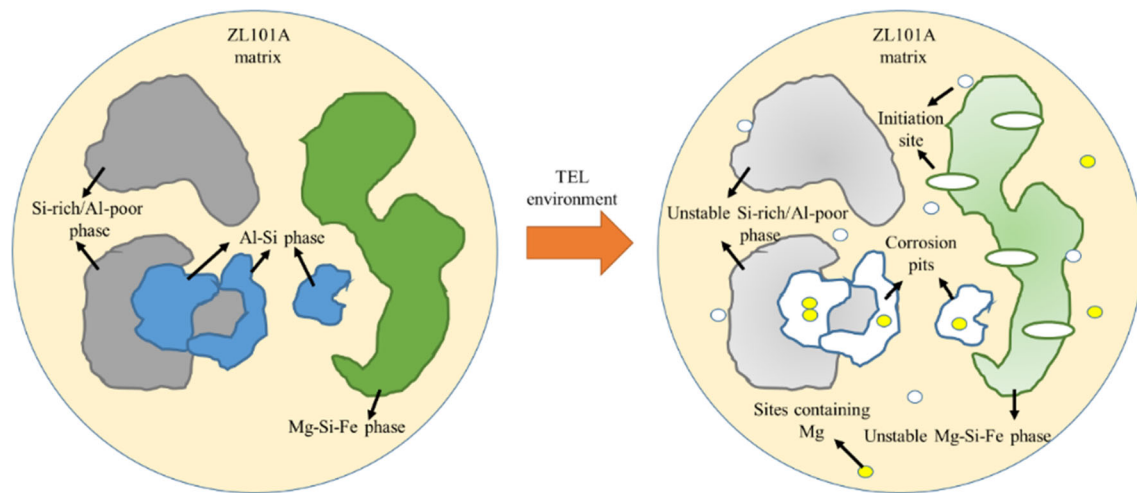


**Fig. 14** Schematic diagram of the pitting corrosion of the ZL101A aluminum alloys in the TEL environment

related to the existence of Mg and high proportion of Al in Al–Si phase.

Both Si-rich/Al-poor phase and Mg–Si–Fe phase were confirmed as the cathode compared with the matrix through the in-situ SKPFM tests, and the Volta potential difference between the two second phases and the matrix can cause the local galvanic corrosion. Mg–Si–Fe phase presented a reduced stability with time, which was mainly attributed to existence of Mg and Fe. The Volta potential difference between the Si-rich/Al-poor phase and the matrix presents an unapparent variation, indicating that the Si-rich/Al-poor phase has a high electrochemical stability.

**Acknowledgments** The authors wish to acknowledgment the National Science and Technology Resources Investigation Program of China (Grant No. 2019FY101400).

**Author Contributions** XD: Visualization, Methodology, Writing—original draft. Zhen Liu: Investigation. QL: Investigation. TZ: Conceptualization, Writing—review & editing. CL: Conceptualization, Supervision, Funding acquisition.

**Data availability** The raw/processed data required to reproduce these findings cannot be fully shared at this time as the data also forms part of an ongoing study.

## Declarations

**Competing Interest** The authors declared that no conflict of interest exists for this work.

## References

1. Wang, L.; Liang, J.; Li, H.; Cheng, L.; Cui, Z.: Quantitative study of the corrosion evolution and stress corrosion cracking of high

strength aluminum alloys in solution and thin electrolyte layer containing Cl<sup>-</sup>. *Corros. Sci.* **178**, 109076 (2021)

2. Ge, F.; Wang, L.; Dou, Y.; Wei, J.; Cheng, L.; Wang, X.; Cui, Z.: Elucidating the passivation kinetics and surface film chemistry of 254SMO stainless steel for chimney construction in simulated desulfurized flue gas condensates. *Constr. Build. Mater.* **285**, 122905 (2021)
3. Tian, H.; Fan, L.; Li, Y.; Pang, K.; Chu, F.; Wang, X.; Cui, Z.: Effect of NH<sub>4</sub><sup>+</sup> on the pitting corrosion behavior of 316 stainless steel in the chloride environment. *J. Electroanal. Chem.* **894**, 115368 (2021)
4. Pu, J.; Zhang, Y.; Zhang, X.; Yuan, X.; Ren, P.; Jin, Z.: Mapping the fretting corrosion behaviors of 6082 aluminum alloy in 3.5% NaCl solution. *Wear* **482–483**, 203975 (2021)
5. Wang, T.; Yang, L.; Tang, Z.; Liu, C.; Ma, Y.; Wu, L.; Yan, H.; Yu, Z.; Liu, W.: Effect of aging treatment on microstructure, mechanical and corrosion properties of 7055 aluminum alloy prepared using powder by-product. *Mater. Sci. Eng. A* **822**, 141606 (2021)
6. Y. Zhang, Y. Chen, Y. Zhang, G. Bian, C. Wang, A. Wang. Initial corrosion behavior and mechanism of 7B04 aluminum alloy under acid immersion and salt spray environments. *Chinese J. Aeronaut.* (2021)-In press.
7. Prabhuraj, P.; Rajakumar, S.: Experimental investigation on corrosion behavior of friction stir welded AA7075-T651 aluminium alloy under 3.5% wt NaCl environment. *Mater. Today Proc.* **45**, 5878–5885 (2021)
8. Kumar, S.R.; Krishnaa, S.D.; Krishna, M.D.; Gokulkumar, N.T.; Akilesh, A.R.: Investigation on corrosion behaviour of aluminium 6061–T6 alloy in acidic, alkaline and salt medium. *Mater. Today Proc.* **45**, 1878–1881 (2021)
9. Zhao, Q.; Guo, C.; Niu, K.; Zhao, J.; Huang, Y.; Li, X.: Long-term corrosion behavior of the 7A85 aluminum alloy in an industrial-marine atmospheric environment. *J. Market. Res.* **12**, 1350–1359 (2021)
10. Zhou, T.; Neding, B.; Lin, S.; Tseng, J.; Hedström, P.: Cu precipitation-mediated formation of reverted austenite during ageing of a 15–5 PH stainless steel. *Scripta Mater.* **202**, 114007 (2021)
11. Welborn, S.S.; Simafranca, A.; Wang, Z.; Wei, H.; Detsi, E.: Chelation-mediated synthesis of nanoporous gold at near-neutral pH and room temperature by free corrosion dealloying of gold-copper alloy driven by oxygen reduction. *Scripta Mater.* **200**, 113901 (2021)

12. Hou, Y.; Xiong, G.; Liu, L.; Li, G.; Moelans, N.; Guo, M.: Effects of  $\text{LaAlO}_3$  and  $\text{La}_2\text{O}_2\text{S}$  inclusions on the initialization of localized corrosion of pipeline steels in NaCl solution. *Scripta Mater.* **177**, 151–156 (2020)
13. Dou, Y.; Han, S.; Wang, L.; Wang, X.; Cui, Z.: Characterization of the passive properties of 254SMO stainless steel in simulated desulfurized flue gas condensates by electrochemical analysis, XPS and ToF-SIMS. *Corros. Sci.* **165**, 108405 (2020)
14. Li, M.; Seyeux, A.; Wiame, F.; Marcus, P.; Światowska, J.: Insights on the Al-Cu-Fe-Mn intermetallic particles induced pitting corrosion of Al-Cu-Li alloy. *Corros. Sci.* **176**, 109040 (2020)
15. Hou, Y.; Wang, J.; Liu, L.; Li, G.; Zhai, D.: Mechanism of pitting corrosion induced by inclusions in Al-Ti-Mg deoxidized high strength pipeline steel. *Micron* **138**, 102898 (2020)
16. Su, H.; Wei, S.; Liang, Y.; Wang, Y.; Wang, B.; Yuan, Y.: Pitting behaviors of low-alloy high strength steel in neutral 3.5 wt% NaCl solution based on in situ observations. *J. Electroanal. Chem.* **863**, 114056 (2020)
17. Cao, C.; Chen, D.; Ren, J.; Shen, J.; Meng, L.; Liu, J.: Improved strength and enhanced pitting corrosion resistance of Al-Mn alloy with Zr addition. *Mater. Lett.* **255**, 126535 (2019)
18. Kadowaki, M.; Muto, I.; Takahashi, K.; Doi, T.; Masuda, H.; Katayama, H.; Kawano, K.; Sugawara, Y.; Hara, N.: Anodic polarization characteristics and electrochemical properties of  $\text{Fe}_3\text{C}$  in chloride solutions. *J. Electrochem. Soc.* **166**, 345–351 (2019)
19. Zhao, K.; Liu, J.; Yu, M.; Li, S.: Through-thickness inhomogeneity of precipitate distribution and pitting corrosion behavior of Al-Li alloy thick plate. *Trans. Nonferr. Metal. Soc.* **29**, 1793–1802 (2019)
20. Revilla, R.I.; Terryn, H.; De Graeve, I.: On the use of SKPFM for in situ studies of the repassivation of the native oxide film on aluminium in air. *Electrochem. Commun.* **93**, 162–165 (2018)
21. Rahimi, E.; Rafsanjani-Abbasi, A.; Imani, A.; Hosseinpour, S.; Davoodi, A.: Correlation of surface Volta potential with galvanic corrosion initiation sites in solid-state welded Ti-Cu bimetal using AFM-SKPFM. *Corros. Sci.* **140**, 30–39 (2018)
22. Guillaumin, V.; Mankowski, G.: Localized corrosion of 6056 T6 aluminium alloy in chloride media. *Corros. Sci.* **42**, 105–125 (2000)
23. Eckermann, F.; Suter, T.; Uggowitz, P.J.; Afseth, A.; Schmutz, P.: Investigation of the exfoliation-like attack mechanism in relation to Al-Mg-Si alloy microstructure. *Corros. Sci.* **50**, 2085–2093 (2008)
24. Esfahani, Z.; Rahimi, E.; Sarvghad, M.; Rafsanjani-Abbasi, A.; Davoodi, A.: Correlation between the histogram and power spectral density analysis of AFM and SKPFM images in an AA7023/AA5083 FSW joint. *J. Alloy Compd.* **744**, 174–181 (2018)
25. Kong, D.; Ni, X.; Dong, C.; Lei, X.; Zhang, L.; Man, C.; Yao, J.; Cheng, X.; Li, X.: Bio-functional and anti-corrosive 3D printing 316L stainless steel fabricated by selective laser melting. *Mater. Design.* **152**, 88–101 (2018)
26. Örnek, C.; Engelberg, D.L.: SKPFM measured Volta potential correlated with strain localisation in microstructure to understand corrosion susceptibility of cold-rolled grade 2205 duplex stainless steel. *Corros. Sci.* **99**, 164–171 (2015)
27. Rohwerder, M.; Turcu, F.: High-resolution Kelvin probe microscopy in corrosion science: scanning Kelvin probe force microscopy (SKPFM) versus classical scanning Kelvin probe (SKP). *Electrochim. Acta.* **53**, 290–299 (2007)
28. Na, K.; Pyun, S.: Effect of sulphate and molybdate ions on pitting corrosion of aluminium by using electrochemical noise analysis. *J. Electroanal. Chem.* **596**, 7–12 (2006)
29. Cai, C.; Zhang, Z.; Cao, F.; Gao, Z.; Zhang, J.; Cao, C.: Analysis of pitting corrosion behavior of pure Al in sodium chloride solution with the wavelet technique. *J. Electroanal. Chem.* **578**, 143–150 (2005)
30. Li, L.; Chen, S.H.; Yang, X.G.; Wang, C.; Guo, W.J.: Pitting corrosion induced current oscillations during electrodisolution of Al in  $\text{HClO}_4$  solutions. *J. Electroanal. Chem.* **572**, 41–49 (2004)
31. Sarvghad-Moghaddam, M.; Parvizi, R.; Davoodi, A.; Haddad-Sabzevar, M.; Imani, A.: Establishing a correlation between interfacial microstructures and corrosion initiation sites in Al/Cu joints by SEM-EDS and AFM-SKPFM. *Corros. Sci.* **79**, 148–158 (2014)
32. Amin, M.A.: Uniform and pitting corrosion events induced by  $\text{SCN}^-$  anions on Al alloys surfaces and the effect of UV light. *Electrochim. Acta.* **56**, 2518–2531 (2011)
33. Sathirachinda, N.; Pettersson, R.; Wessman, S.; Pan, J.: Study of nobility of chromium nitrides in isothermally aged duplex stainless steels by using SKPFM and SEM/EDS. *Corros. Sci.* **52**, 179–186 (2010)
34. Trueba, M.; Trasatti, S.P.: Study of Al alloy corrosion in neutral NaCl by the pitting scan technique. *Mater. Chem. Phys.* **121**, 523–533 (2010)
35. Nakhaie, D.; Davoodi, A.; Imani, A.: The role of constituent phases on corrosion initiation of NiAl bronze in acidic media studied by SEM-EDS, AFM and SKPFM. *Corros. Sci.* **80**, 104–110 (2014)
36. Sabzi, M.; Dezfali, S.M.; Balak, Z.: Crystalline texture evolution, control of the tribocorrosion behavior, and significant enhancement of the abrasion properties of a Ni-P nanocomposite coating enhanced by zirconia nanoparticles. *Int. J. Miner. Metall. Mater.* **26**, 1020–1030 (2019)
37. Dezfali, S.M.; Sabzi, M.: Deposition of self-healing thin films by the sol-gel method: a review of layer-deposition mechanisms and activation of self-healing mechanisms. *Appl. Phys. A.* **125**, 577 (2019)
38. Sabzi, M.; Far, S.M.; Dezfali, S.M.: Effect of melting temperature on microstructural evolutions, behavior and corrosion morphology of Hadfield austenitic manganese steel in the casting process. *Int. J. Miner. Metall. Mater.* **25**, 1431–1438 (2018)
39. Mousavi Anijdan, S.H.; Sabzi, M.; Asadian, M.; Jafarian, H.R.: Effect of sub-layer temperature during HFCVD process on morphology and corrosion behavior of tungsten carbide coating. *Int. J. Appl. Ceram. Technol.* **16**, 243–253 (2019)
40. Wang, P.; Ma, L.; Cheng, X.; Li, X.: Influence of grain refinement on the corrosion behavior of metallic materials: A review. *Int. J. Miner. Metall. Mater.* **28**, 1112–1126 (2021)

